Dalton
Transactions

PAPER

View Article Online
View Journal | View Issue

Cite this: *Dalton Trans.*, 2019, **48**, 15560

Spin state solvomorphism in a series of rare S = 1 manganese(III) complexes†

Andrew Barker,‡[a] Conor T. Kelly, ‡[a] Irina A. Kühne, [a] Stephen Hill, [b,c] J. Krzystek, [b] Paul Wix, [d] Kane Esien,[e] Solveig Felton, [e] Helge Müller-Bunz[a] and Grace G. Morgan *[a]

Received 11th June 2019,
Accepted 16th July 2019

DOI: 10.1039/c9dt02476j

rsc.li/dalton

Structural, magnetic and spectroscopic data of four complex salts, [Mn(napsal$_2$323)]NTf$_2$, **1**,[Mn(napsal$_2$323)]ClO$_4$, **2**, [Mn(napsal$_2$323)]BF$_4$, **3** and [Mn(napsal$_2$323)]NO$_3$, **4**, of the [Mn(napsal$_2$323)]$^+$ complex cation indicate that the Mn^{3+} ion is stabilized in the rare S = 1 spin triplet form in this ligand sphere. Zero-field splitting values of D = +19.6 cm^{-1} and $|E|$ = 2.02 cm^{-1} for complex **1** were obtained by High Field Electron Paramagnetic Resonance (HFEPR) measurements conducted over a range of frequencies. Structural and magnetic data also indicate that co-crystallization of complexes **2** and **3** with 0.5 equivalents of ethanol yields the high spin S = 2 forms of the perchlorate and tetrafluoroborate solvates [Mn(napsal$_2$323)]ClO$_4$·0.5(C$_2$H$_5$OH), **2·0.5EtOH** and [Mn(napsal$_2$323)]BF$_4$·0.5(C$_2$H$_5$OH), **3·0.5EtOH**.

Introduction

Manipulation of spin states in transition metal elements offers an interesting route to spintronic applications.[1–5] Many d^n configurations can have more than one arrangement of spins, fully unpaired being the most common, Table 1, but alternative fully paired or partially paired configurations are also possible in d^4–d^7 ions. Thermal switching between high spin (HS) and low spin (LS) forms is well known and much studied in Fe^{2+} and Fe^{3+} complexes. Transitions between the intermediate spin (IS) and either the HS[6] or LS[7] state in Fe^{3+} are also known but are much less common. A smaller number of Co^{2+} complexes also show thermal spin state switching, in this case always between the fully paired and fully unpaired arrangements, Table 1.[8,9] Thermal spin state switching is also now relatively well established in some Mn^{3+} complexes where the transition is always between the S = 1 IS and the S = 2 HS states.[10–19]

However, although thermal switching between spin triplet and quintet states is possible in Mn^{3+}, by far the majority of reported molecular and solid state compounds with this ion are HS *i.e.* they obey Hund's first rule of maximum spin multiplicity. This makes the S = 1 state something of a chemical and magnetic rarity with less than twenty reported Mn^{3+} complexes in the spin triplet form at room temperature. These S = 1 examples can be broadly sorted into four categories: [Mn(CN)$_6$]$^{3-}$ complexes with different counter cations;[20–24] porphyrin[25–28] or cyclam[29] type ligands with axially coordinated ligands such as cyanide; poly(pyrazolyl)borate type complexes;[30–33] and a smattering of others which are less easily categorized including those with tris (quinone) oximate ligands,[34] or carboxylate donors.[35] The triplet form of Mn^{3+} thus represents a less-prevalent building block in molecular magnetism and one which is worthy of further investigation, both as a potential single ion magnet (SIM), or as a starting point for thermal or non-thermal spin state switching to the quintet form at or above room temperature.

We now report four new Mn^{3+} compounds, all salts of the [Mn(napsal$_2$323)]$^+$ complex cation, which are fully or predominantly in the rare S = 1 state at room temperature. The ligand napsal$_2$323 is a Schiff base resulting from condensation of 1,2-

Table 1 High spin (HS), intermediate spin (IS) and low spin (LS) S values for d^4–d^7 configurations

d^4 Mn^{3+}, Cr^{2+}	d^5 Fe^{3+}, Mn^{2+}	d^6 Fe^{2+}, Co^{3+}	d^7 Co^{2+}
HS, S = 2	HS, S = 5/2	HS, S = 2	HS, S = 3/2
IS, S = 1	IS, S = 3/2	IS, S = 1	—
LS, S = 0	LS, S = 1/2	LS, S = 0	LS, S = 1/2

---

[a] School of Chemistry, University College Dublin (UCD), Belfield, Dublin 4, Ireland. E-mail: grace.morgan@ucd.ie
[b] National High Magnetic Field Laboratory, Florida State University, Tallahassee, FL 32310, USA
[c] Department of Physics, Florida State University, Tallahassee, FL 32306, USA
[d] School of Chemistry & CRANN Institute, Trinity College Dublin, University of Dublin, College Green, Dublin 2, Ireland
[e] Centre for Nanostructured Media (CNM), School of Mathematics and Physics, Queen's University Belfast, Belfast, BT7 1NN, UK

† Electronic supplementary information (ESI) available. CCDC 1921981, 1921978, 1921977, 1921979 and 1921980. For ESI and crystallographic data in CIF or other electronic format see DOI: 10.1039/c9dt02476j

‡ These authors contributed equally to the work.

bis(3-aminopropylamino)ethane with 2-hydroxy-1-naphthaldehyde which we have abbreviated as napsal$_2$323 to indicate the 323 alkyl connectivity in the starting tetraamine and the presence of a napthol donor. [Mn(napsal$_2$323)]$^+$ belongs to the [Mn(R-sal$_2$323)]$^+$ series of Schiff base complexes of which other members have been shown to exhibit thermal spin crossover.[11–16] However, with previously reported ligands in the series, Mn^{3+} is almost always in the HS state at room temperature or shows a variation of spin state for the same complex cation with different counterions. In contrast the larger naphthol donor groups in the ligand used here stabilize the [Mn(napsal$_2$323)]$^+$ cation in the S = 1 state in all the (solvate-free) crystalline lattices which were examined. Co-crystallization with ethanol however disrupts the packing and allows access to the S = 2 state in the perchlorate and tetrafluoroborate cases. This illustrates that solvomorphs of the [Mn(napsal$_2$323)]$^+$ complex can stabilize different internal electronic arrangements and hence different magnetic states.

Results and discussion

Synthesis

Preparation of the bistriflimide (NTf$_2^-$), perchlorate (ClO$_4^-$), tetrafluoroborate (BF$_4^-$) and nitrate (NO$_3^-$) salts of [Mn(napsal$_2$323)]$^+$ was achieved in a one-pot reaction, Table 2, where different exchange salts (AX) were used to prepare four different salts of the complex cation, as well as solvates of two of these salts, those of **2** and **3**, Table 2.

Magnetic characterisation of unsolvated (S = 1) complexes

Variable temperature magnetic susceptibility of polycrystalline samples of unsolvated complexes **1–4** was recorded on a Quantum Design MPMS XL SQUID between 2 K and 300 K, Fig. 1.

For each of the complexes **1–4** a value close to $\chi_M T$ = 1.00 cm^3 K mol^{-1} is observed across most of the measured range, with all complexes showing a slight upturn close to room temperature suggesting onset of a gradual thermal spin crossover. In the perchlorate complex **2** the $\chi_M T$ value starts to rise already by 110 K demonstrating the accessibility to the S = 2 state for Mn^{3+} in this coordination sphere. Below 20 K a characteristic drop is observed due to zero field splitting.

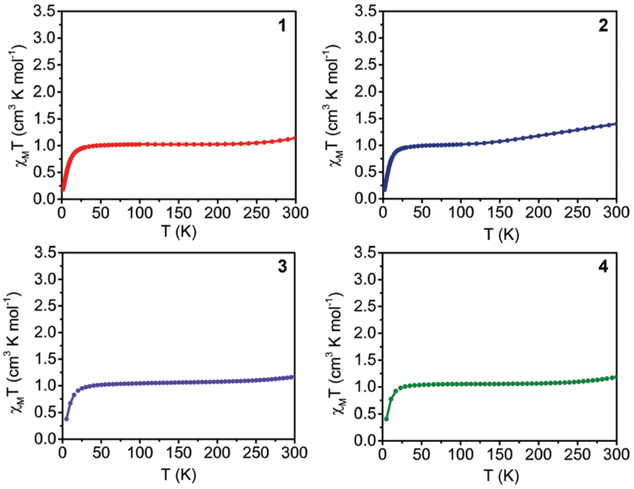

Fig. 1 Plots of $\chi_M T$ *vs.* T for complexes **1–4** from 2 K to 300 K indicating that they exist in an intermediate spin state (S = 1) up to room temperature.

Table 2 Synthesis of complexes **1–4**, and solvates **2·0.5EtOH** and **3·0.5EtOH**. AX is the exchange salt where A is NH$_4^+$, K$^+$ or Na$^+$ and X is NTf$_2^-$ (**1**), ClO$_4^-$ (**2**), BF$_4^-$ (**3**) or NO$_3^-$ (**4**)

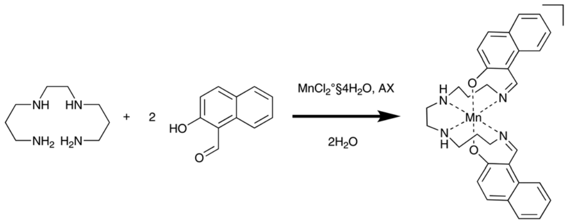

Complex	Molecular formula
1	[Mn(napsal$_2$323)]NTf$_2$
2	[Mn(napsal$_2$323)]ClO$_4$
2·0.5EtOH	[Mn(napsal$_2$323)]ClO$_4$·0.5(C$_2$H$_5$OH)
3	[Mn(napsal$_2$323)]BF$_4$
3·0.5EtOH	[Mn(napsal$_2$323)]BF$_4$·0.5(C$_2$H$_5$OH)
4	[Mn(napsal$_2$323)]NO$_3$

High field electron paramagnetic resonance spectra of 1

Given the paucity of data on zero field splitting parameters in spin triplet Mn^{3+} complexes,[31,36] it was of interest to record High Field EPR (HFEPR) spectra in order to investigate the nature of the anisotropy. Spectra were typically very weak in intensity so only complex **1** was studied in detail. Measurements were carried out on a powdered sample at 4.5 K and 10 K in the frequency range from 203 to 634 GHz. Representative spectra (along with simulations) recorded at frequencies of 406.4 and 203.2 GHz are displayed in Fig. 2 and S2,† respectively.

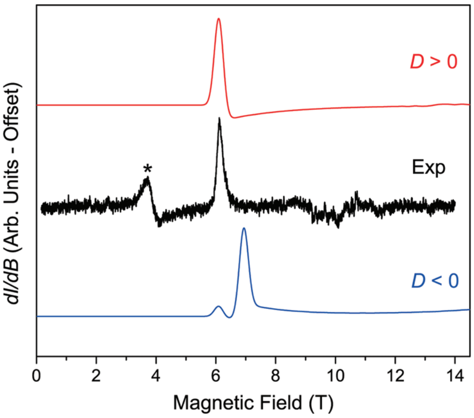

Fig. 2 Powder EPR spectrum (recorded in derivative mode, dI/dB, where I is the transmitted signal intensity) of **1** recorded at 4.5 K and 406.4 GHz (black trace), along with spectral simulations assuming a powder distribution for the two crystallites, for both signs of D (see text). * is trace impurity.

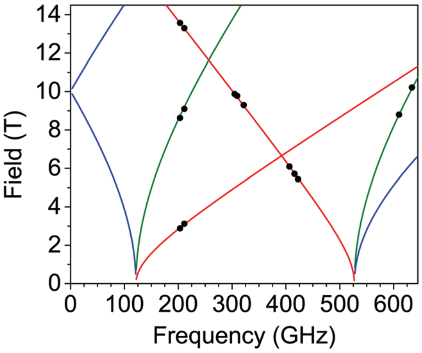

Fig. 3 2D magnetic field *versus* frequency (or quantum energy) map for **1** at 10 K, where the experimental resonances are indicated with black points. The curves are simulations according to a $S = 1$ Hamiltonian (see ESI†), with the colors denoting turning points in the powder spectra for field parallel to *x* (green), *y* (blue), *z* (red).

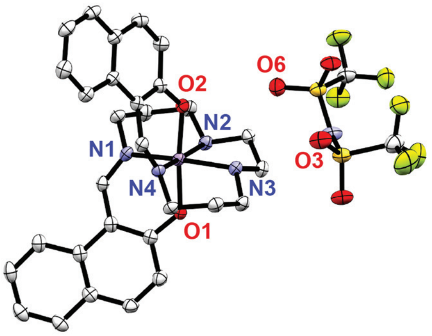

Fig. 4 Structure of **1** recorded at 100 K. Thermal ellipsoids are drawn at 50% atomic probability. Hydrogen atoms have been omitted for clarity.

By plotting the observed resonance positions on a 2D magnetic field *versus* frequency plot, Fig. 3, it is found that most of them lie on a family of curves that can be well simulated according to a spin $S = 1$ Hamiltonian given in the ESI.†[37] The best simulation of the combined multi-frequency dataset places very tight constraints on the magnitudes of the axial and rhombic 2nd order zero-field splitting parameters, D and E. The sign of the dominant axial interaction can then be determined by comparing spectral simulations with the experimental ones for both signs of D. As can be seen from Fig. 2 and S2,† a positive D (red trace) accounts very well for several of the observed resonances, although not all of them; by contrast, a negative D (blue trace) results in significant spectral features that are not observed experimentally. Therefore, the simulations unequivocally determine the sign of D to be positive (the sign of E remains undetermined). This was confirmed at other frequencies. The remaining resonances not captured by the $S = 1$ simulations can either be attributed to known weak impurity signals in the EPR probe (see ESI†) or are assumed to be due to traces of the solvated complex.

Spin Hamiltonian parameters D, E and g were fitted to the multifrequency data, with the resulting values $D = +19.6\ \mathrm{cm}^{-1}$, $|E| = 2.02\ \mathrm{cm}^{-1}$ and $g = 2.00$. The zero field splitting parameters observed are in good agreement with those of the two $S = 1$ scorpionate Mn^{3+} complexes published by Forshaw *et al.*,[31] with reported D values of $+17.97\ \mathrm{cm}^{-1}$ and $+15.89\ \mathrm{cm}^{-1}$. This indicates that relatively large zero-field splitting can be expected in the spin triplet forms of Mn^{3+}.

Structural characterisation of unsolvated ($S = 1$) complexes

Single crystal X-ray diffraction at 100 K was used to characterise the structures of **1**, **2** and **4** which agreed well with the powder diffraction data of the bulk samples, Fig. S15.† The molecular structure of **1** is shown in Fig. 4, and the structures of **2** and **4** are given in Fig. S3 and S4† respectively. The asymmetric unit of complexes **1** and **4** comprises one full occupancy cation and one full occupancy anion while that for complex **2** comprises one half occupancy cation and one half occupancy anion, with a twofold rotational (C_2) axis bisecting the pairs of *cis*-imine and *cis*-amine donors. In all cases the geometry around the Mn^{3+} centre is *pseudo*-octahedral, with *cis*-amine, *cis*-imine and *trans*-phenolate donors. The Mn–O and Mn–N bond lengths, Table 3, correspond to expected $S = 1$ values for related complexes.[11–16] Octahedral distortion parameters $\sum$ and Θ are small and closely resemble the range of values previously reported for IS ($S = 1$) Mn^{3+}.[15,38] Comparison of the packing interactions for the unsolvated complexes reveals a 1-D hydrogen bonding network which is common to **1**, **2** and **4**, in which the hydrogens of the amines of the complex cation form hydrogen bonds with bridging oxygens of the respective counter anion, Table S6.† This is illustrated for complex **1** in Fig. 5 and S6,† and for complexes **2** and **4** in Fig. S8 and S11.†

Magnetic characterisation of solvated ($S = 2$) complexes

Given the thermal accessibility of the $S = 2$ state in related complexes[11–16] a natural progression would be to establish if the HS state of complexes **1–4** could be stabilized by further crystal engineering. To this end the synthesis was repeated in a variety of solvents likely to promote extensive hydrogen bonding. Solvent mixtures included undried acetonitrile, ethanol and methanol. Attempts with methanol did yield crystals in some cases but the bulk products were of insufficient purity for further analysis. However attempts with ethanol yielded highly crystalline samples of $[\mathrm{Mn(napsal_2323)}]\mathrm{ClO_4}\cdot0.5(\mathrm{C_2H_5OH})$, **2·0.5EtOH**, and$[\mathrm{Mn(napsal_2323)}]\mathrm{BF_4}\cdot0.5(\mathrm{C_2H_5OH})$, **3·0.5EtOH**. SQUID data on the two solvated complexes shows that in contrast to the unsolvated analogues **2** and **3**, they are fully HS over the measured temperature range 2–300 K, Fig. 6. The small upturn in the $\chi_\mathrm{M}T$ data for **2·0.5EtOH** may indicate ferromagnetic ordering at low temperatures but as the sample was not constrained it may also be due to torquing in the magnetic field on cooling. The stabilization of the high spin $S = 2$ state in the ethanol solvates may be due to the overall increased volume when ethanol is trapped in the lattice which could serve to push the complex cations apart so that they have more space to accommodate the longer Mn–donor bonds which the $S = 2$ state requires. The outcome is that incorporation of ethanol solvate molecules stabilizes the cation in the HS state, indicating that the spin state is highly sensitive to the lattice contents.

Table 3 Selected bond lengths (Å) and distortion parameters (°) for **1**, **2**, **2·0.5EtOH**, **3·0.5EtOH**, and **4**

Complex	1	2	4	5	2·0.5EtOH	3·0.5EtOH
Mn–O(1)	1.8753(19)	1.8855(14)	1.8762(8)	1.8687(13)	1.8679(10)	1.8671(10)
Mn–O(2)	1.870(2)		1.8803(8)	1.8764(13)	1.8635(10)	1.8701(10)
Mn–N(1)$_{\text{imine}}$	1.975(2)	1.9946(17)	1.9876(11)	1.9814(16)	2.0846(12)	2.1211(11)
Mn–N(4)$_{\text{imine}}$	1.978(2)		1.9825(10)	1.9805(16)	2.1143(13)	2.0872(12)
Mn–N(2)$_{\text{amine}}$	2.063(2)	2.0630(17)	2.0548(10)	2.0654(17)	2.2381(13)	2.2398(12)
Mn–N(3)$_{\text{amine}}$	2.058(2)		2.0573(10)	2.0643(17)	2.2429(13)	2.2426(11)
Σ	35.32	30.97	31.27	34.34	71.37	71.25
Θ	97.20	97.07	88.41	96.48	238.81	239.22

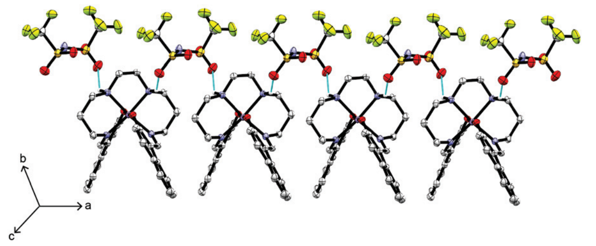

Fig. 5 View of the 1-D hydrogen bonding network in **1**. Thermal ellipsoids are drawn at 50% atomic probability. Hydrogen atoms, except those involved in the hydrogen bonding, have been omitted for clarity.

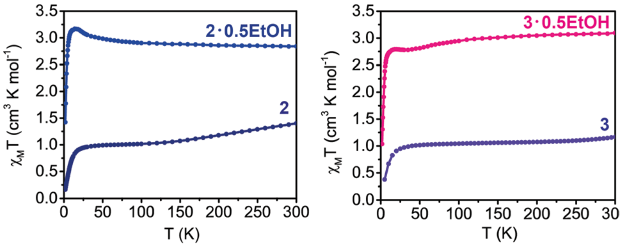

Fig. 6 Plots of $\chi_M T$ *vs.* T for complexes **2** and **2·0.5EtOH** and **3** and **3·0.5EtOH** from 5 K to 300 K illustrating the spin state dependence on lattice solvate molecules.

It is well known that anion[40–42] and solvent[12,17,43–47] affect choice of spin state in SCO complexes, in addition to the effects of local crystal field strength and geometry conferred by the ligand environment. Harding has recently demonstrated the importance of changing solvates in some Fe^{3+} SCO complexes where significant differences in both profile and hysteresis width were observed. In the case of complexes **2** and **3** the effect of co-crystallizing solvent molecules is marked by a complete switch in spin state from triplet to quintet, opening the door to solvent-induced spin state changes in this cation.

Structural characterisation of the solvated (S = 2) complexes

Single crystal X-ray diffraction at 100 K was used to characterise the solvated complexes **2·0.5EtOH** and **3·0.5EtOH** which were found to be isostructural. The structure of **2·0.5EtOH** is shown in Fig. 7 and S4,† and that of **3·0.5EtOH** in Fig. S5.† The asymmetric unit of each contains one full occupancy cation, one full occupancy anion and one half occupancy ethanol solvent molecule, which is disordered over two positions. In both cases, the geometry around the manganese

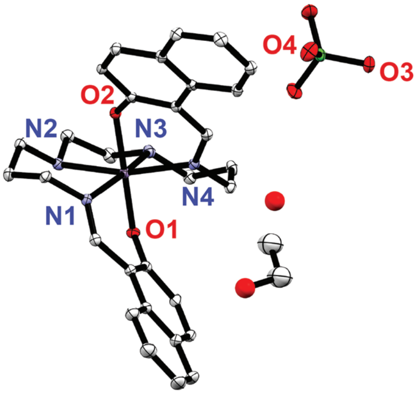

Fig. 7 Structure of **2·0.5EtOH** recorded at 100 K showing cation, anion and disordered half-occupancy ethanol molecule. Thermal ellipsoids are drawn at 50% atomic probability. Hydrogen atoms have been omitted for clarity.

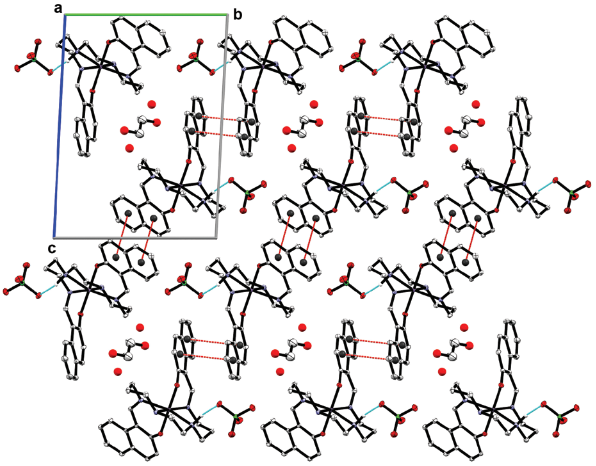

Fig. 8 View of the intermolecular interactions in **2·0.5EtOH**. Hydrogen bonding (blue) occurs between the hydrogen of the amine of the backbone and the oxygen atoms of the ClO_4^- counter anion, and π–π interactions (red) occur between the naphthol rings. See also Fig. S9† and equivalent interactions for **3·0.5EtOH** in Fig. S10.† Thermal ellipsoids are drawn at 50% atomic probability. Hydrogen atoms, except those involved in the hydrogen bonding, have been omitted for clarity.

centre is distorted octahedral, as expected in this *pseudo* Jahn–Teller ion. An expansion of the equatorial Mn–N bonds is observed along with a slight compression of the Mn–O bonds, Table 3. The octahedral distortion parameters $\sum$ and Θ are significantly larger than those of the $S = 1$ unsolvated complexes, presumably due to the increased distortion in the HS state. Hydrogen bonding between the hydrogen of the amine on the ligand backbone and the oxygen of the counter anion is present but there is no chain formation for the interaction as was observed in the unsolvated $S = 1$ analogues **2** and **3**. Instead the hydrogen bonding is discrete between one complex cation and one complex anion, Fig. 8 and S10.† Weak offset π–π interactions (3.67–3.74 Å) between the naphthol rings are also observed which are just within the acceptable margins of 3.3–3.8 Å.[39] The packing of the complexes in both the **2·0.5EtOH** and **3·0.5EtOH** structures results in channels containing the ethanol solvate parallel to the *a* axis.

Conclusions

We have reported a new series of IS ($S = 1$) Mn^{3+} complexes of the $[Mn(napsal_2323)]^+$ cation. HFEPR measurements on the bistriflimide complex **1** to investigate the nature of the magnetic anisotropy yielded values of $D = +19.6\ cm^{-1}$ and $|E| = 2.02\ cm^{-1}$, *i.e.* a large positive zero field splitting in line with previous reports on $S = 1$ Mn^{3+} complexes. Structural information shows a strong 1-D hydrogen bonding network in the IS complexes **1**, **2** and **4**. Co-crystallization with ethanol induced a complete change in spin state from $S = 1$ to $S = 2$ in the ClO_4^- and BF_4^- salts **2·0.5EtOH** and **3·0.5EtOH**. The 1-D hydrogen bonding network is also broken in the solvated lattices, which may assist the change of spin state to the larger volume spin quintet form. Our work on studying the prevalence and stability of the $S = 1$ state in this, and related complex cations, continues and will include investigation of the effect of different solvate molecules on the resultant Mn^{3+} spin state.

Experimental

Synthetic procedures

Synthesis of $[Mn(napsal_2323)]NTf_2$, 1. 2-Hydroxy-1-naphthaldehyde (0.344 g, 2 mmol) was dissolved in acetonitrile (10 mL) and stirred for 10 minutes at room temperature. Neat 1,2-bis(3-aminopropylamino)ethane (165 μL, 1 mmol) was added to this solution and a bright yellow colour was immediately observed. The solution was filtered and manganese(II) chloride tetrahydrate (0.197 g, 1 mmol) and neat triethylamine (265 μL, 2 mmol) were added, causing the colour to change to dark green. Solid lithium bis(trifluoromethanesulfonyl)imide (0.287 g, 1 mmol) was added and the solution was stirred overnight. The dark green solution was then filtered and crystals suitable for X-ray crystallography were formed by slow evaporation of solvent. Yield: 0.080 g (10%). Elemental analysis, calculated for $[C_{30}H_{32}N_4O_2Mn](CF_3SO_2)_2N$, theory % (found %): C 46.34 (46.00), H 4.07 (3.73), N 8.44 (8.21).

Infrared spectroscopy (FT-ATR) ν/cm^{-1}: 3260 (w), 3060 (w), 2960 (w), 2934 (w), 2899 (w), 2879 (w), 1619 (m), 1596 (m), 1539 (m), 1468 (w), 1451 (w), 1431 (w), 1406 (w), 1337 (s), 1321 (s), 1307 (m), 1260 (w), 1225 (m), 1184 (s), 1129 (s), 1084 (m), 1054 (s), 1009 (m), 991 (m), 964 (m), 948 (m), 864 (w), 821 (s), 791 (m), 746 (s), 654 (m), 599 (s), 570 (s), 503 (s), 466 (m), 428 (m).

UV-Vis (MeCN) λ_{max}/nm ($\varepsilon_{max}/L\ mol^{-1}\ cm^{-1}$): 230.0 (61 200), 307.4 (18 800), 540.5 (970), 592.2 (780).

Synthesis of $[Mn(napsal_2323)]ClO_4$, 2. The procedure for **1** was repeated except sodium perchlorate (0.122 g, 1 mmol) was used in place of the lithium bis(trifluoromethanesulfonyl)imide. Yield: 0.138 g (21%). Elemental analysis, calculated for $[C_{30}H_{32}N_4O_2Mn]ClO_4$, theory % (found %): C 56.75 (56.32), H 5.08 (4.90), N 8.82 (8.52).

Infrared spectroscopy (FT-ATR) ν/cm^{-1}: 3674 (w), 3248 (w), 2970 (w), 2929 (w), 2901 (w), 2866 (w), 1623 (s), 1596 (m), 1545 (m), 1470 (m), 1441 (s), 1386 (m), 1343 (w), 1278 (s), 1241 (w), 1207 (w), 1150 (w), 1074 (s), 1052 (s), 986 (m), 976 (m), 933 (m), 909 (m), 866 (s), 817 (w), 791 (m), 768 (s), 621 (s), 564 (m), 522 (w), 454 (w), 432 (m).

UV-Vis (MeCN) λ_{max}/nm ($\varepsilon_{max}/L\ mol^{-1}\ cm^{-1}$): 230.0 (68 200), 307.5 (20 800), 542.5 (1000), 592.4 (860).

Synthesis of $[Mn(napsal_2323)]BF_4$, 3. The procedure for **1** was repeated except ammonium tetrafluoroborate (0.104 g, 1 mmol) was used in place of the lithium bis(trifluoromethanesulfonyl)imide. Yield: 0.104 g (32%). Elemental analysis, calculated for $[C_{30}H_{32}N_4O_2Mn]BF_4$, theory % (found %): C 57.90 (58.09), H 5.18 (5.23), N 9.00 (8.62).

Infrared spectroscopy (FT-ATR) ν/cm^{-1}: 3250 (w), 2958 (w), 2929 (w), 2911 (w), 2866 (w), 1614 (m), 1594 (s), 1537 (m), 1504 (m), 1449 (m), 1431 (s), 1392 (m), 1358 (m), 1339 (s), 1305 (m), 1258 (m), 1194 (m), 1121 (w), 1068 (s), 1025 (s), 1007 (s), 991 (s), 966 (s), 942 (m), 911 (w), 862 (w), 825 (s), 744 (s), 648 (w), 605 (s), 560 (w), 515 (s), 466 (m), 432 (w), 420 (w).

UV-Vis (MeCN) λ_{max}/nm ($\varepsilon_{max}/L\ mol^{-1}\ cm^{-1}$): 230.0 (59 900), 307.8 (18 800), 540.4 (520), 592.9 (420).

Synthesis of $[Mn(napsal_2323)]NO_3$ (4). The procedure for **1** was repeated except manganese(II) nitrate tetrahydrate (0.251 g, 1 mmol) was used in place of the manganese(II) chloride and lithium bis(trifluoromethanesulfonyl)imide. Yield: 0.090 g (15%). Elemental analysis, calculated for $[C_{30}H_{32}N_4O_2Mn]NO_3$, theory % (found %): C 60.30 (60.35), H 5.40 (5.70), N 11.72 (11.38).

Infrared spectroscopy (FT-ATR) ν/cm^{-1}: 3154 (w), 2936 (w), 2909 (w), 2864 (w), 1612 (m), 1592 (s), 1535 (s), 1504 (m), 1431 (s), 1372 (s), 1325 (s), 1302 (s), 1254 (s), 1192 (s), 1145 (m), 1086 (s), 1031 (s), 995 (m), 966 (m), 907 (w), 864 (m), 825 (s), 748 (s), 646 (w), 605 (s), 556 (m), 522 (s), 469 (m), 426 (m).

UV-Vis (MeCN) λ_{max}/nm ($\varepsilon_{max}/L\ mol^{-1}\ cm^{-1}$): 229.4 (79 000), 304.3 (23 600), 540.8 (1200), 592.0 (960).

Synthesis of $[Mn(napsal_2323)]ClO_4·0.5EtOH$ (2·0.5EtOH). The procedure for **1** was repeated except sodium perchlorate (0.122 g, 1 mmol) was used in place of the lithium bis (trifluoromethanesulfonyl)imide. Additionally, a 1 : 1 mixture of acetonitrile/ethanol was used instead of pure acetonitrile. Yield: 0.176 g (26%). Elemental analysis, calculated for $[C_{30}H_{32}N_4O_2Mn]ClO_4{\cdot}0.5(C_2H_5OH)$, theory % (found %): C 56.58 (56.32), H 5.36 (4.97), N 8.51 (8.63).

Infrared spectroscopy (FT-ATR) ν/cm^{-1}: 3258 (w), 2926 (w), 2866 (w), 1617 (m), 1602 (s), 1545 (m), 1506 (w), 1451 (m), 1409 (w), 1360 (w), 1337 (m), 1288 (m), 1262 (m), 1190 (m), 1143 (w), 1078 (s), 1058 (s), 995 (m), 944 (s), 909 (m), 858 (m), 825 (s), 778 (w), 750 (s), 683 (w), 646 (w), 621 (s), 605 (s), 540 (w), 501 (m), 454 (w), 418 (m).

UV-Vis (MeCN) $\lambda_{\max}/\mathrm{nm}$ ($\varepsilon_{\max}/\mathrm{L\ mol^{-1}\ cm^{-1}}$): 230.2 (72 100), 307.2 (22 200), 542.0 (1100), 592.2 (870).

Synthesis of [Mn(napsal$_2$323)]BF$_4$·0.5EtOH (3·0.5EtOH). The procedure for **1** was repeated except ammonium tetrafluoroborate (0.104 g, 1 mmol) was used in place of the lithium bis (trifluoromethanesulfonyl)imide. Additionally, a 1 : 1 mixture of acetonitrile/ethanol was used instead of pure acetonitrile. Yield: 0.078 g (12%). Elemental analysis, calculated for $[C_{30}H_{32}N_4O_2Mn]BF_4{\cdot}0.5(C_2H_5OH)$, theory % (found %): C 57.69 (57.77), H 5.47 (5.36), N 8.68 (8.59).

Infrared spectroscopy (FT-ATR) ν/cm^{-1}: 3356.2 (w), 3256.3 (w), 3056.5 (w), 2960.7 (w), 2919.9 (w), 2866.9 (w), 1616.9 (m), 1594.5 (s), 1539.5 (s), 1504.8 (m), 1464.0 (w), 1449.7 (m), 1431.4 (s), 1390.6 (m), 1358.0 (w), 1339.6 (s), 1302.9 (s), 1260.1 (m), 1213.2 (w), 1194.9 (m), 1158.2 (w), 1143.9 (m), 1125.5 (w), 1088.8 (s), 1078.6 (s), 1052.1 (s), 1035.8 (s), 993.0 (m), 944.1 (w), 876.8 (m), 862.5 (m), 825.8 (s), 748.3 (s), 646.4 (w), 605.6 (s), 558.7 (w), 515.9 (m), 483.2 (w), 466.9 (w), 422.1 (m).

UV-Vis (MeCN) $\lambda_{\max}/\mathrm{nm}$ ($\varepsilon_{\max}/\mathrm{L\ mol^{-1}\ cm^{-1}}$): 230.0 (78 300), 307.0 (24 200), 541.0 (1200), 592.9 (900).

Conflicts of interest

There are no conflicts to declare.

Acknowledgements

We thank Science Foundation Ireland (SFI) for generous support of an Investigator Project Award (12/IP/1703 to G. G. M). This research was also supported by the Irish Research Council GOIPG/2018/2510 (C. T. K.), GOIPG/2015/2713 (P. W.), GOIPD/2016/503 (I. A. K.), US Department of Energy DE-SC0019330 (S. H.), EU COST Actions CA15128 Molecular Spintronics (MOLSPIN), CM1305, Explicit Control over Spin-states in Technology and Biochemistry (ECOSTBio) and CA15107 Multi-Functional Nano-Carbon Composite Materials Network (MultiComp). We also thank University College Dublin (UCD) for their generous support *via* award of a UCD Advance PhD Supplemental Funding Grant (C. T. K. and G. G. M.). A portion of this work was performed at the National High Magnetic Field Laboratory, which is supported by the National Science Foundation Cooperative Agreement No. DMR-1644779 and the State of Florida. This work was also supported through award of an RSC Research Mobility Grant from the Royal Society of Chemistry (RSC) (I. A. K.).

Notes and references

1 H. Song, M. A. Reed and T. Lee, *Adv. Mater.*, 2011, **23**, 1583–1608.

2 K. Senthil Kumar and M. Ruben, *Coord. Chem. Rev.*, 2017, **346**, 176–205.

3 S. K. Kuppusamy, B. Heinrich, J. Arabski, G. Schmerber, M. Bowen, S. Boukari, E. Beaurepaire, J. Dreiser and M. Ruben, *Adv. Mater.*, 2018, 1705416.

4 O. Kahn and C. J. Martinez, *Science*, 1998, **279**, 44–48.

5 F. Schleicher, M. Studniarek, S. K. Kuppusamy, E. Urbain, K. Katcko, J. Chen, T. Frauhammer, M. Hervé, U. Halisdemir, L. M. Kandpal, D. Lacour, A. Riminucci, L. Joly, F. Scheurer, B. Gobaut, F. Choueikani, E. Otero, P. Ohresser, J. Arabski, G. Schmerber, W. Wulfhekel, E. Beaurepaire, W. Weber, S. Boukari, M. Ruben and M. Bowen, *ACS Appl. Mater. Interfaces*, 2018, **10**, 31580–31585.

6 S. Mossin, B. L. Tran, D. Adhikari, M. Pink, F. W. Heinemann, J. Sutter, R. K. Szilagyi, K. Meyer, D. J. Mindiola and J. Am, *Chem. Soc.*, 2012, **134**, 13651–13661.

7 W. O. Koch, V. Schünemann, M. Gerdan, A. X. Trautwein and H.-J. Krüger, *Chem. – Eur. J.*, 1998, **4**, 686–691.

8 M. G. Cowan, J. Olguín, S. Narayanaswamy, J. L. Tallon and S. Brooker, *J. Am. Chem. Soc.*, 2011, **134**, 2892–2894.

9 S. Hayami, K. Murata, D. Urakami, Y. Kojima, M. Akita and K. Inoue, *Chem. Commun.*, 2008, 6510–6512.

10 P. G. Sim and E. Sinn, *J. Am. Chem. Soc.*, 1981, **103**, 241–243.

11 G. G. Morgan, K. D. Murnaghan, H. Müller-Bunz, V. McKee and C. J. Harding, *Angew. Chem., Int. Ed.*, 2006, **45**, 7192–7195.

12 K. Pandurangan, B. Gildea, C. Murray, C. J. Harding, H. Müller-Bunz and G. G. Morgan, *Chem. – Eur. J.*, 2012, **18**, 2021–2029.

13 A. J. Fitzpatrick, E. Trzop, H. Müller-Bunz, M. M. Dîrtu, Y. Garcia, E. Collet and G. G. Morgan, *Chem. Commun.*, 2015, **51**, 17540–17543.

14 P. N. Martinho, B. Gildea, M. M. Harris, T. Lemma, A. D. Naik, H. Müller-Bunz, T. E. Keyes, Y. Garcia and G. G. Morgan, *Angew. Chem., Int. Ed.*, 2012, **51**, 12597–12601.

15 B. Gildea, M. M. Harris, L. C. Gavin, C. A. Murray, Y. Ortin, H. Müller-Bunz, C. J. Harding, Y. Lan, A. K. Powell and G. G. Morgan, *Inorg. Chem.*, 2014, **53**, 6022–6033.

16 B. Gildea, L. C. Gavin, C. A. Murray, H. Müller-Bunz, C. J. Harding and G. G. Morgan, *Supramol. Chem.*, 2012, **24**, 641–653.

17 J. Sirirak, D. J. Harding, P. Harding, K. S. Murray, B. Moubaraki, L. Liu and S. G. Telfer, *Eur. J. Inorg. Chem.*, 2015, **2015**, 2534–2542.

18 Z. Liu, S. Liang, X. Di and J. Zhang, *Inorg. Chem. Commun.*, 2008, **11**, 783–786.

19 S. Wang, M. Ferbinteanu, C. Marinescu, A. Dobrinescu, Q.-D. Ling and W. Huang, *Inorg. Chem.*, 2010, **49**, 9839–9851.

20 R. F. Ziolo, R. H. Stanford, G. R. Rossman and H. B. Gray, *J. Am. Chem. Soc.*, 1974, **96**, 7910–7915.

21 J. J. Alexander and H. B. Gray, *J. Am. Chem. Soc.*, 1968, **90**, 4260–4271.

22 I. D. Chawla and M. J. Frank, *J. Inorg. Nucl. Chem.*, 1970, **32**, 555–563.

23 W. P. Griffith, *Coord. Chem. Rev.*, 1975, **17**, 177–247.

24 W. E. Buschmann, L. Liable-Sands, A. L. Rheingold and J. S. Miller, *Inorg. Chim. Acta*, 1999, **284**, 175–179.

25 H. Homborg, L. Galich and H. Hu, *J. Porphyrins Phthalocyanines*, 1998, **2**, 79–87.

26 J. T. Landrum, K. Hatano, W. Robert Scheldt and C. A. Reed, *J. Am. Chem. Soc.*, 1980, **102**, 6729–6735.

27 A. P. Hansen and H. M. Goff, *Inorg. Chem.*, 1984, **23**, 4519–4525.

28 M. Matsuda, J.-I. Yamaura, H. Tajima and T. Inabe, *Chem. Lett.*, 2005, **34**, 1524–1525.

29 S. Mossin, H. O. Sørensen and H. Weihe, *Acta Crystallogr., Sect. C: Cryst. Struct. Commun.*, 2002, **58**, m204–m206.

30 H. E. Colmer, C. G. Margarit, J. M. Smith, T. A. Jackson and J. Telser, *Eur. J. Inorg. Chem.*, 2016, **2016**, 2413–2423.

31 A. P. Forshaw, J. M. Smith, A. Ozarowski, J. Krzystek, D. Smirnov, S. A. Zvyagin, T. D. Harris, H. I. Karunadasa, J. M. Zadrozny, A. Schnegg, K. Holldack, T. A. Jackson, A. Alamiri, D. M. Barnes and J. Telser, *Inorg. Chem.*, 2013, **52**, 144–159.

32 F. Hossain, M. A. Rigsby, C. T. Duncan, P. L. Milligan, R. L. Lord, M. Baik and F. A. Schultz, *Inorg. Chem.*, 2007, **46**, 2596–2603.

33 D. C. L. De Alwis and F. A. Schultz, *Inorg. Chem.*, 2003, **42**, 3616–3622.

34 P. Basu and A. Chakravorty, *Inorg. Chem.*, 1992, **31**, 4980–4986.

35 S. Ganguly, S. Karmakar and A. Chakravorty, *Inorg. Chem.*, 1997, **36**, 116–118.

36 C. Duboc, *Chem. Soc. Rev.*, 2016, **45**, 5834–5847.

37 J. Krzystek, A. Ozarowski and J. Telser, *Coord. Chem. Rev.*, 2006, **250**, 2308–2324.

38 A. J. Fitzpatrick, S. Stepanovic, H. Müller-Bunz, M. A. Gruden-Pavlović, P. García-Fernández and G. G. Morgan, *Dalton Trans.*, 2016, **45**, 6702–6708.

39 C. Janiak, *Dalton Trans.*, 2000, 3885–3896.

40 S. Sundaresan, I. A. Kühne, C. T. Kelly, A. Barker, D. Salley, H. Müller-Bunz, A. K. Powell, G. G. Morgan, S. Sundaresan, I. A. Kühne, C. T. Kelly, A. Barker, D. Salley, H. Müller-Bunz, A. K. Powell and G. G. Morgan, *Crystals*, 2018, **9**, 19.

41 S. Hayami, K. Hiki, T. Kawahara, Y. Maeda, D. Urakami, K. Inoue, M. Ohama, S. Kawata and O. Sato, *Chem. – Eur. J.*, 2009, **15**, 3497–3508.

42 I. Nemec, R. Herchel, R. Boĉa, Z. Trávníĉek, I. Svoboda, H. Fuess and W. Linert, *Dalton Trans.*, 2011, **40**, 10090–10099.

43 D. Sertphon, P. Harding, K. Murray, B. Moubaraki, S. Neville, L. Liu, S. Telfer and D. Harding, *Crystals*, 2019, **9**, 116.

44 A. Malliaris and V. Papaefthimiou, *Inorg. Chem.*, 1982, **21**, 770–774.

45 I. A. Gass, S. Tewary, G. Rajaraman, M. Asadi, D. W. Lupton, B. Moubaraki, G. Chastanet, J.-F. Létard and K. S. Murray, *Inorg. Chem.*, 2014, **53**, 5055–5066.

46 M. Hostettler, K. W. Törnroos, D. Chernyshov, B. Vangdal and H.-B. Bürgi, *Angew. Chem., Int. Ed.*, 2004, **43**, 4589–4594.

47 W. Phonsri, P. Harding, L. Liu, S. G. Telfer, K. S. Murray, B. Moubaraki, T. M. Ross, G. N. L. Jameson and D. J. Harding, *Chem. Sci.*, 2017, **8**, 3949–3959.